The objective of the current study is to design a non-equiatomic FeMnNiTiAlSiC high entropy steel with a dual-phase structure having better mechanical properties as compared to conventional steel, high entropy steel, and Fe-based HEAs. However, introducing a small amount of intermetallics into the alloy would facilitate a reasonable amount of strength. In the present investigation alloying behaviour with progressive milling, thermal stability, and phases formed after sintering were studied. Further, the structure and microstructure of the SPSed HES were studied in detail. The mechanical properties such as microhardness, elastic modulus, and compressive strength of the high entropy steel were also ascertained and the enhancement in these properties was understood with the help of strengthening mechanisms.

5.1 Melting point prediction of the alloy

The machine learning (ML) approach, rule of mixture, and CALPHAD were used to calculate the melting point of the HES3, and its calculation detail was mentioned in subsection 2.3.1. The values of the melting point through ML, rule of mixture, and CALPHAD were found to be 1388 ℃ (1661 K), 1378 ℃ (1651 K), and 1200 ℃ (1473 K), respectively. It was observed from the previous literature on the HEAs [229], that the theoretical melting point (through the ML approach) was very much close to the experimental findings.

5.2 Alloying behaviour of milled powder sample

Figure 5.1 shows the XRD patterns of milled powder samples at various milling times. The XRD pattern clearly shows the diffraction peaks of all the corresponding elements in the pre-mixed powders i.e., Fe (a = 0.286 nm; cI2), α-Mn (a = 0.891 nm; cI58), Ni (a = 0.352 nm; cF4), Ti (a = b = 0.295 nm and c = 0.468 nm; hP2), Al (a = 0.404 nm; cF4), Si (a = 0.543 nm; cF8) and C (a = b = 0.245 nm and c = 0.670 nm; hP4). The intensity of all the individual peaks decreases with the increased in milling time, which is evident from Figure 5.1. After 5 h of milling the peaks

corresponding to C disappear. The peaks of Al vanished within 10 h of milling. The diffraction peaks of Ni, Mn, Ti, and higher angle peaks of Si disappeared as the milling progressed to 15 h. The alloying rate of the individual elements inversely depends upon the melting point and ductility of the elements. The elements having lower melting point shows a higher

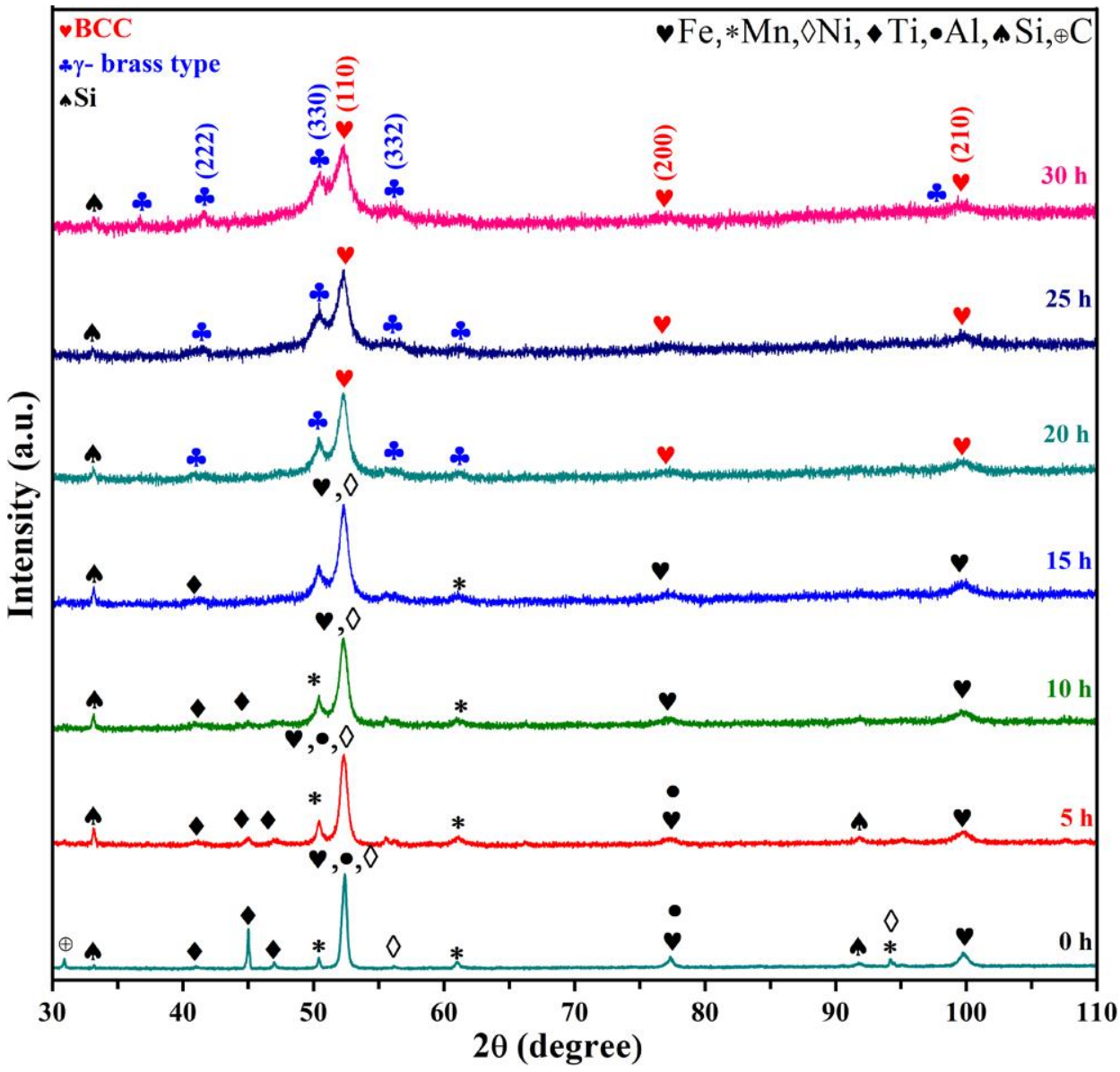

Figure 5.1: XRD pattern of the HES3 powder at various milling time. The dual-phase formed during the milling consist of BCC (a = 0.287 nm) and γ-brass type (a = 0.890 nm) structure along with undissolved silicon.

diffusion coefficient than the elements having higher melting point. It was observed that C disappeared first as compared to other alloying elements which might be due to its smaller atomic radius. Ti dissolved earlier than, Fe due to the lower diffusion coefficient as compared to Fe. However, Si remained undissolved even after 30 h of milling. The XRD pattern of 20 h milled powder shown in Figure 5.1 discerned the presence of metastable phases like BCC (host lattice α-Fe) and γ-brass type (Cu_5Zn_8) structure with undissolved Si. The milling time was increased further up to 30 h to see if any change in phases formed or not. However, no phase change occurred except that the amount of undissolved Si was decreased. It is evident from Figure 5.1, that the dual-phase structure of BCC (a = 0.287 nm, cI2) and γ-brass type (a = 0.890 nm, cI52) structure was formed with a trace amount of Si after 30 h of milling. Figures 5.2(a, b, and c) display the Rietveld refinement of 20 h, 25 h, and 30 h milled powder samples, respectively.

The Rietveld refinement (GSAS II software) is used to calculate the crystallite size and lattice strain of the milled samples at 20 h, 25 h, and 30 h, which is listed in Table 5.1. It was observed that the crystallite size was decreased as the milling time increased. The values of the crystallite size are found in the range of ~13-23 nm and ~11-17 nm for BCC and γ-brass type phase, respectively. The milling time increased from 20 h to 30 h the crystallite size for Si was decreased from 31 nm to 22 nm. The effect of milling time (20 h to 30 h) on the lattice strain was analysed and it was an increased trend from 0.72 - 1.0, 0.66 - 1.49, and 0.25 – 0.59 for BCC, γ-brass type, and Si, respectively. The atomic size mismatch between the individual elements, mechanical deformation in the powder particles, and the increase in the fraction of grain boundary are the reasons behind the increase of lattice strain with the increase in milling time. Further, it was also observed that the decrease in the diffraction peak intensity and peak broadening occurred as milling time was increased (Figure 5.2(a and b)). This was due to the lattice distortion during the milling

process, which led to induced lattice strain and extra grain refinement. The usual behaviour of the milling process and the combination of both phenomena contribute to the peak broadening. There was a slight variation in the amount of phase fraction for the BCC, γ-brass type structure with milling time was observed. The dislocation density showed a negligible change with the milling time and it was explained in previously reported composites, quasicrystals, and HEAs [276–278]. The values of the phase fraction, crystallite size, lattice strain, and dislocation density are listed in Table 5.1.

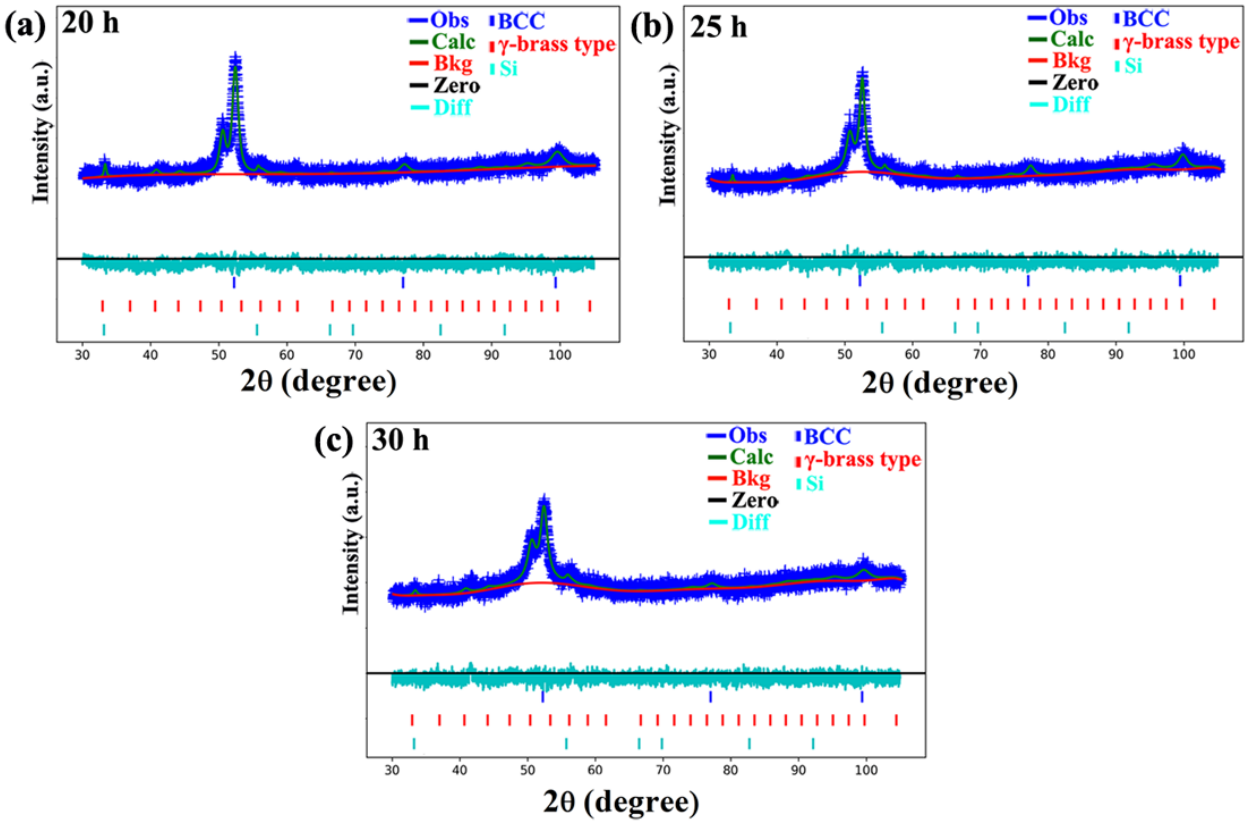

Figure 5.2: Rietveld refinement of XRD patterns of milled powder at (a) 20 h; wR = 2.716 %, GoF = 1.07, and $\varkappa^2$ = 1.15, (b) 25 h; wR = 2.637 %, GoF = 1.07, and $\varkappa^2$ = 1.15, (c) 30 h; wR = 2.596 %, GoF = 1.06, and $\varkappa^2$ = 1.12.

Table 5.1: Variation in phase fraction, crystallite size, microstrain, lattice parameter, and dislocation density during milling.

S.No.	Sample Designation	Phases	Phase Fraction (%)	Lattice Parameter (nm)	Crystallite Size (nm)	Micro strain	Dislocation Density (m^{-2})
1	20 h	BCC	73.7	0.287	23	0.72	0.94×10^{18}
		γ -brass type	21.1	0.890	17	0.66	----
		Si	5.2	0.543	31	0.25	----
2	25 h	BCC	69.1	0.287	17	0.96	1.17×10^{18}
		γ -brass type	26.1	0.890	12	1.11	----
		Si	4.8	0.543	29	0.26	----
3	30 h	BCC	67.6	0.287	13	1.00	2.54×10^{18}
		γ -brass type	28.4	0.890	11	1.49	----
		Si	4	0.543	22	0.60	----

5.3 TEM analysis of the powder sample

A transmission electron microscope (TEM) was used to analyse the structural and nanostructured behaviour of the 30 h milled powder sample of the HES3. Figure 5.3(a) and (b) illustrate the bright field and the corresponding SAED pattern of milled powder, respectively.

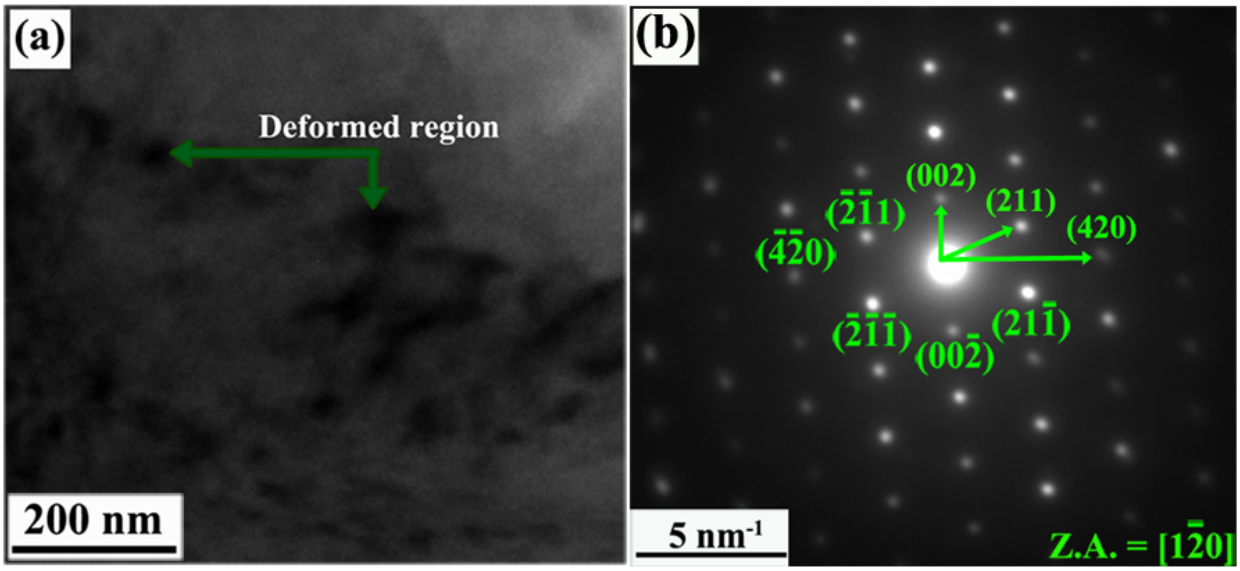

Figure 5.3: The TEM micrographs of as-milled powder showing (a) bright-field image; (b) corresponding selected area electron diffraction spot pattern.

The bright-field image showed the deformation in 30 h milled powder and the formation of nanostructured grains with a size of less than 15 nm. It was analysed from the selected area diffraction pattern (Figure 5.3(b)) that the γ-brass type structure was formed in the milled powder sample. The diffraction spots corresponding to the (211), (002), and (420) reflection of the γ-brass type phase along [1$\bar{2}$0] zone axis was observed in the SAED. The 30 h milled powder sample showed the nanocrystalline grains were formed, which is ~12 nm in size. The irregular dark patches were observed in the bright field image, which may be the remanence of high lattice strain accumulated during the mechanical alloying. It was also confirmed from Table 5.1 that the lattice strain calculated from the Rietveld refinement was relatively high and it was found to be 1.49 for γ-brass type structure. This observation was also seen in the XRD pattern of milled samples (shown in Figure 5.1).

5.4 Surface morphology of the mechanically alloyed sample

The SEM micrographs at different milling times of 30 h milled powder were shown in Figure 5.4(a-d). The morphological features of milled powder samples are sizeable river patterns on the surfaces that can be discerned. This type of morphological feature may be attributed to repeated fracture and continuous deformation during milling. Figure 5.4(e) display the EDS spectrum of full area, which is marked in Figure 5.4(d). Figure 5.4(f) shows the particle size distribution (histogram) of milled powder.

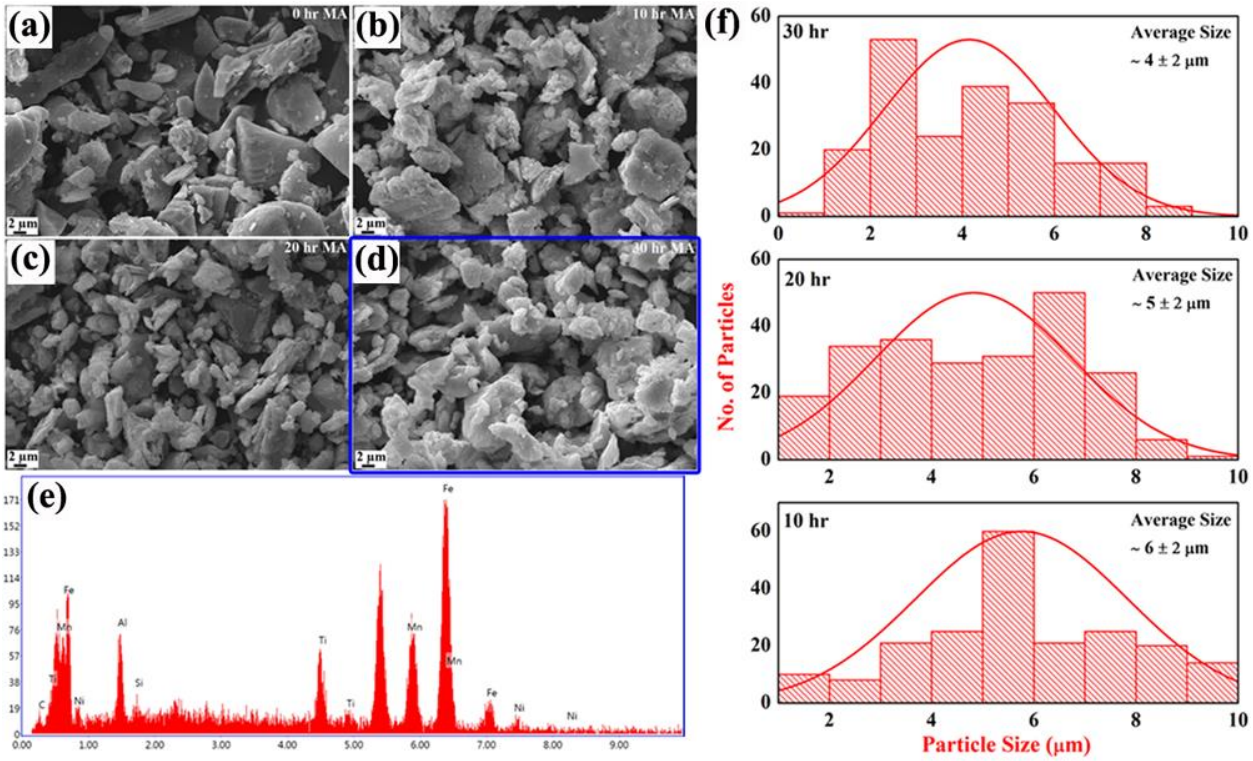

Figure 5.4: The size and shape of the powder particle at (a) 0 h; (b) 10 h; (c) 20 h; (d) 30 h and full area for EDS, and (e) EDS spectrum of the full area. The SEM micrographs exhibit sizeable river pattern on the surfaces. The distribution of the particle size of powder particles at different milling duration (f).

The ImageJ software was used to determine the particle size of the 30 h milled powder from the SEM micrograph. It was observed that the milled powder was of different sizes and shapes, varying

from 1-10 µm. The average particle size decreased with the milling time and the values were found to be ~ 6 ± 2 µm, 5 ± 2 µm, and 4 ± 2 µm for 10 h, 20 h, and 30 h, respectively. The region selected for area elemental mapping revealed that the BCC phase is predominantly rich in Fe, while the gamma brass type structure is Mn-rich, which is displayed in Figure 5.5. This also confirmed the dual-phase structure formation in the milled powder sample, which is observed from the XRD analysis of the 30 h sample.

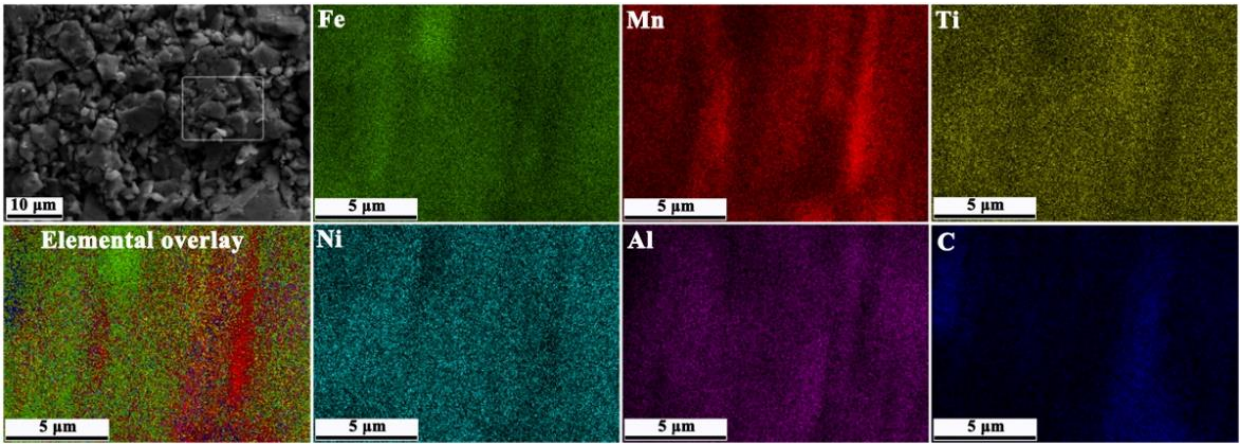

Figure 5.5: Area elemental mapping of 30 h of milled powder green compact sample of HES3.

5.5 Thermal stability of mechanically alloyed sample

To study the thermal stability of the non-equiatomic high entropy steel after the milling was done using the DSC. Figure 5.6 illustrates the DSC thermogram of the alloy ranging from 200 ℃ to 1000 ℃ with 20 K/min of heating rate. It was evident from the DSC thermogram (Figure 5.6). that four exothermic events were present at 520 ℃, 690 ℃, 860 ℃, and 1000 ℃. To understand the dynamics of phase transformation in the present alloy system the milled powder sample was annealed at various temperatures. The diffraction patterns of the milled powder annealed at 500 ℃, 600 ℃, 900 ℃, and 1100 ℃, as displayed in Figure 5.7. At R.T. the alloy consists of a BCC and γ-brass type structure with a minor fraction of Si. The milled powder is thermally stable up to

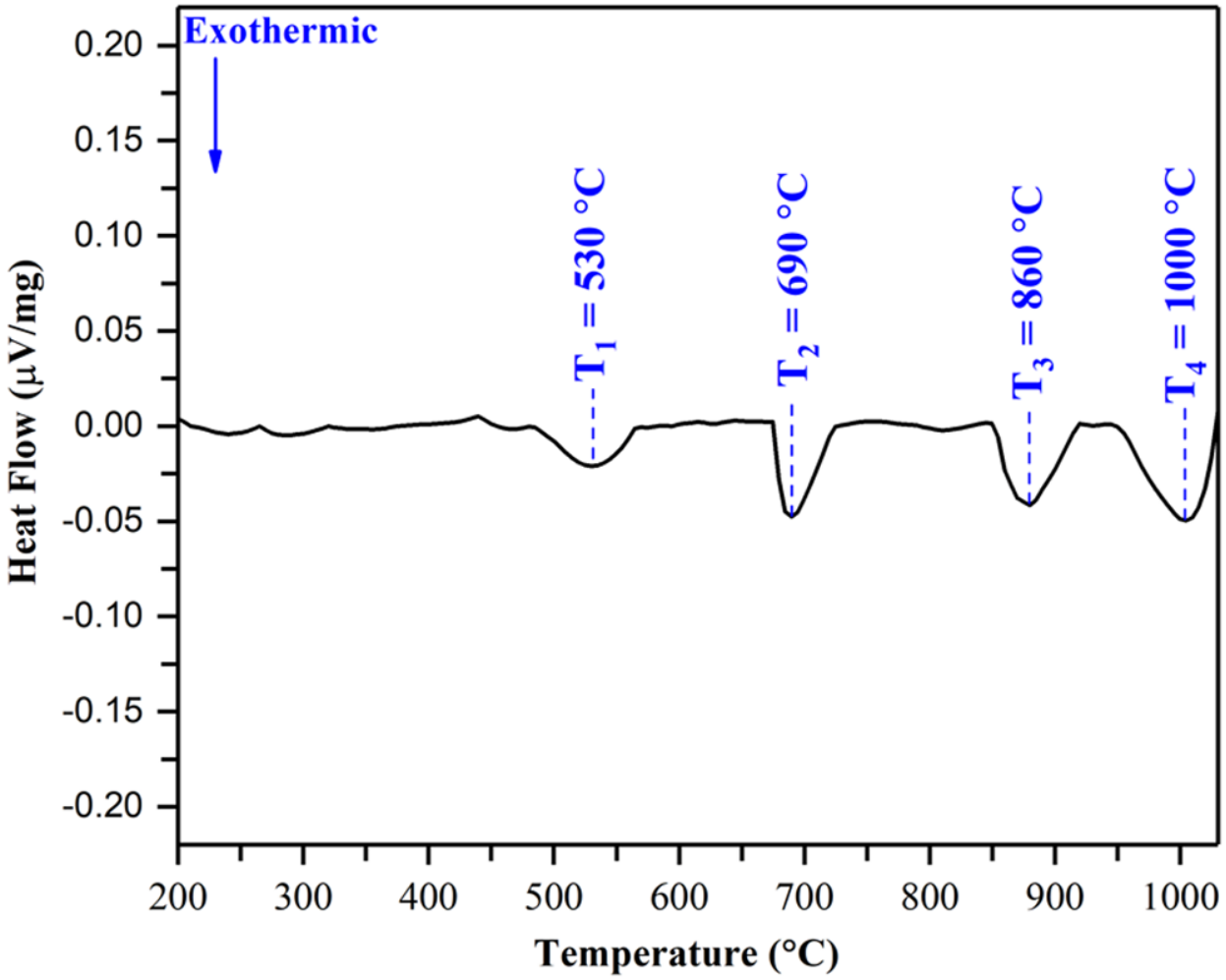

Figure 5.6: DSC thermogram of 30 h milled powder of non-equiatomic FeMnNiTiAlSiC high entropy steel heated up to 1050 °C. The figure shows the phase transformation occurs at T_1, T_2, T_3 and T_4.

500 ℃, as no additional diffraction peaks corresponding to any phase transformation are evident (Figure 5.6 and 5.7). At 600 ℃, the additional diffraction peaks corresponding to the ordering of the γ-brass type structure were evident. This type of gamma brass (also known as χ-type) precipitates formation in $Fe_{36}Cr_{12}Mo_{10-x}Ti_x$ (x = 0, 2, 4…., 10 at. %) alloys was also observed [279]. They have seen that by adding Ti the formation of χ-type precipitate was shifted towards lower temperature [279]. Similarly, in Ti-containing HES the ordering or texturing was shifted by adding Ti (higher melting point element), which was not present in HES1 alloy. In between 600

°C and 900 °C the parent, BCC phase was retained but the γ-brass type structure dissolved, and the FCC phase (a = 0.362 nm, cF4) evolved as the major phase along with some intermetallic compounds i.e., TiC (a = 0.431 nm, cF8) and Fe_5Si_3 type (a = b = 0.678 nm, c = 0.475 nm, hP16).

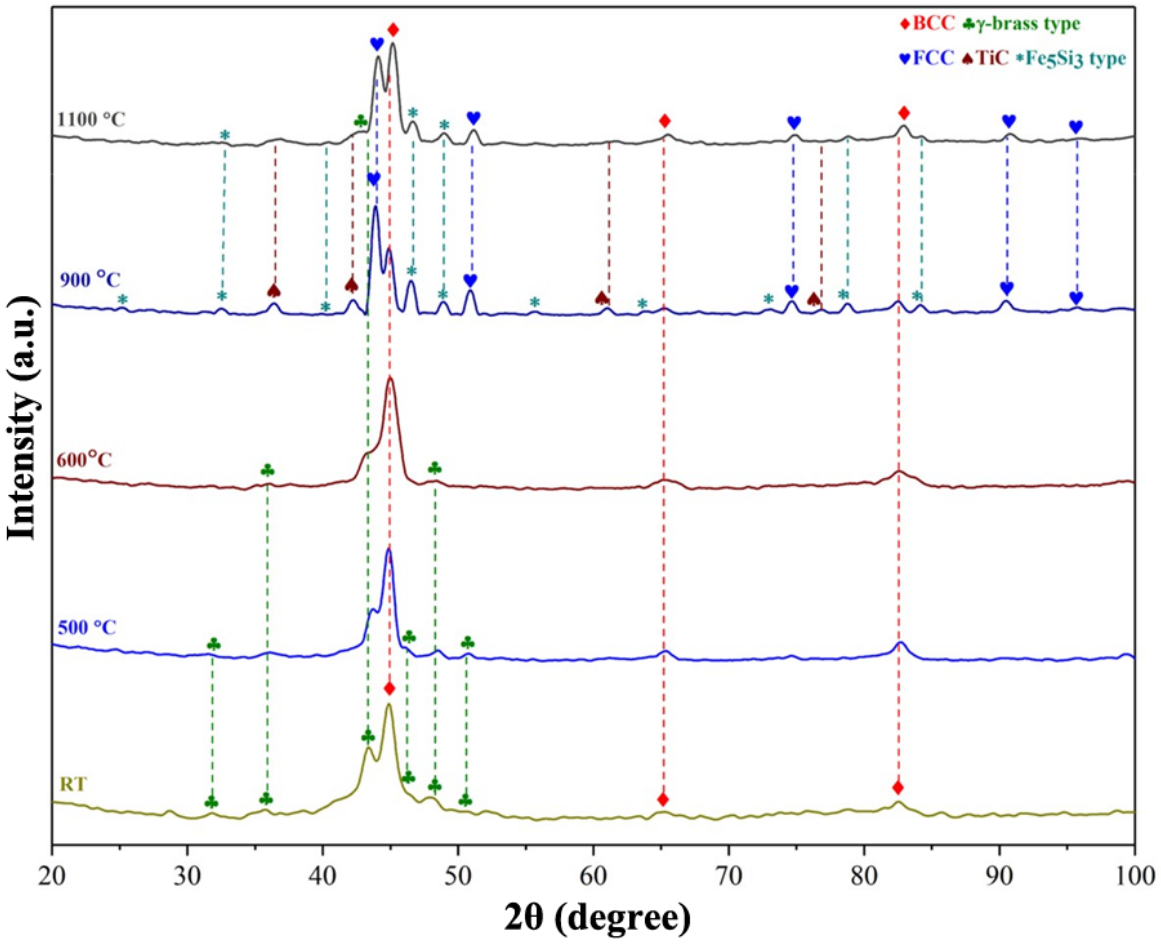

Figure 5.7: XRD pattern representing the phases formed during annealing of 30 h milled powder at temperature of 500 °C, 600 °C, 900 °C and 1100 °C. The phases formed were FCC solid solution along with the intermetallics Fe_5Si_3 type and TiC (in between 600 °C - 900 °C). XRD pattern of the 1100 °C exhibits the change in the amount of phase fraction of the BCC and FCC.

However, further increased the temperature to 1100 °C, the amount of the BCC and FCC phase considerably changes. The phase fraction and lattice parameter of annealed powder samples at different temperature conditions are listed in Table 5.2.

Table 5.2: Phase fraction and lattice parameter of the phases formed in the annealed sample at various temperatures and the SPSed sample.

Condition	Phases	Phase Fraction (%)	Lattice Parameter (nm)
500 ℃	BCC	67.80	0.287
	γ -brass type	32.20	0.890
600 ℃	BCC	63.90	0.287
	γ -brass type	36.10	0.890
900 ℃	BCC	30.50	0.287
	FCC	50.10	0.362
	Fe_5Si_3 type	15.70	a = b = 0.678, c = 0.475
	TiC	3.50	0.431
1100 ℃	BCC	55.40	0.287
	FCC	31.40	0.362
	Fe_5Si_3 type	10.0	a = b = 0.678, c = 0.475
	TiC	3.0	0.431
SPSed	FCC	58.00	0.362
	B2-type	21.40	0.290
	TiC	11.10	0.431
	Fe_5Si_3 type	9.50	a = b = 0.678, c = 0.475

5.6 Structural analysis of the SPSed sample

Figure 5.8(a) represents the XRD pattern of non-equiatomic high entropy steel after the spark plasma sintering (SPS).

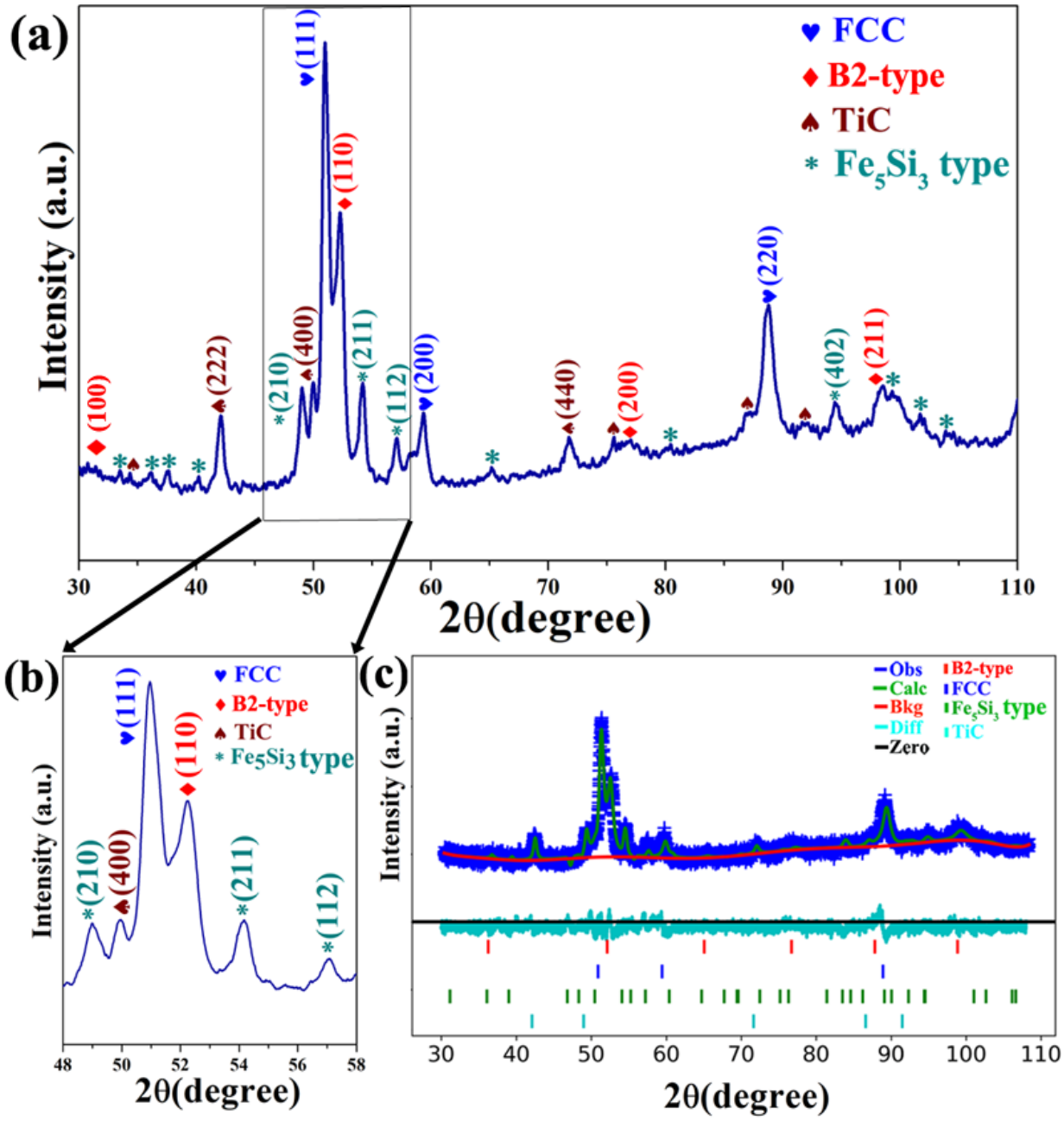

Figure 5.8: (a) XRD pattern of SPSed sample; (b) Enlarge view of the marked area between 48^0-58^0; (c) Rietveld refinement of XRD pattern of SPSed sample of the HES3; wR = 3.145 %, GoF = 1.32 and $\varkappa^2$ = 1.75. The phases formed after the sintering (SPS) were FCC as the major phase, B2-type as secondary phase along with the intermetallics TiC and Fe_5Si_3 type.

The enlarged view of the diffraction peak along the (111) plane in between 48^0 - 58^0, and the Rietveld refinement of the SPSed sample, as shown in Figure 5.8(b and c), respectively. The XRD

pattern of the SPSed sample (Figure 5.8(a)) discerns the presence of dual-phase structure having a major FCC (a = 0.362 nm) phase and a minor B2-type (a = 0.290 nm) phase along with some intermetallics i.e., Fe_5Si_3 type (a = b = 0.678 nm, c = 0.475 nm) and TiC (a = 0.431 nm). Table 5.2 lists the phase fraction and lattice parameter of the SPSed sample.

5.7 Microstructural and chemical analysis of the SPSed analysis

Figure 5.9(a and b) shows the SEM micrographs of SPSed samples at different magnifications. The micrographs clearly show the different contrast areas, the white, light, and dark grey regions along with black spots. The light and dark grey contrast features are related to the FCC and B2-type phases, respectively. Similarly, the white and black contrast corresponds to TiC and Fe_5Si_3 type intermetallic, respectively. The surface morphology appears to be irregular in shape and size. The area marked for EDS at full region and point EDS is shown in Figure 5.9(b). The elemental distribution of the full area EDS is displayed in Figure 5.9(c). The dark grey region is rich in Fe, Al, and Ni, which is related to the B2-type, and the light grey region is rich in Fe, Mn, and Ni, which is related to the FCC solid solution. The point EDS at different locations of the SPSed sample is listed in Table 5.3. Figure 5.10 displays the elemental distribution and elemental overlay

Table 5.3: Elemental composition of SPSed sample of the non-equiatomic FeMnNiTiAlSiC high entropy steel at point EDS.

Elemental composition (at. %)							
Sample condition	**Scan area**	**Fe**	**Mn**	**Ni**	**Ti**	**Al**	**Si**
SPSed sample	**Spot 1**	47.30	19.60	15.10	2.60	8.20	7.20
	Spot 2	33.20	8.40	20.30	5.4	27.50	5.20

of the SPSed sample. It can be inferred from the EDS and the mapping result that the SPSed sample was chemically homogenous. The dual-phase structure after the SPS is also validated by the point EDS and elemental mapping of the SPSed sample of the HES.

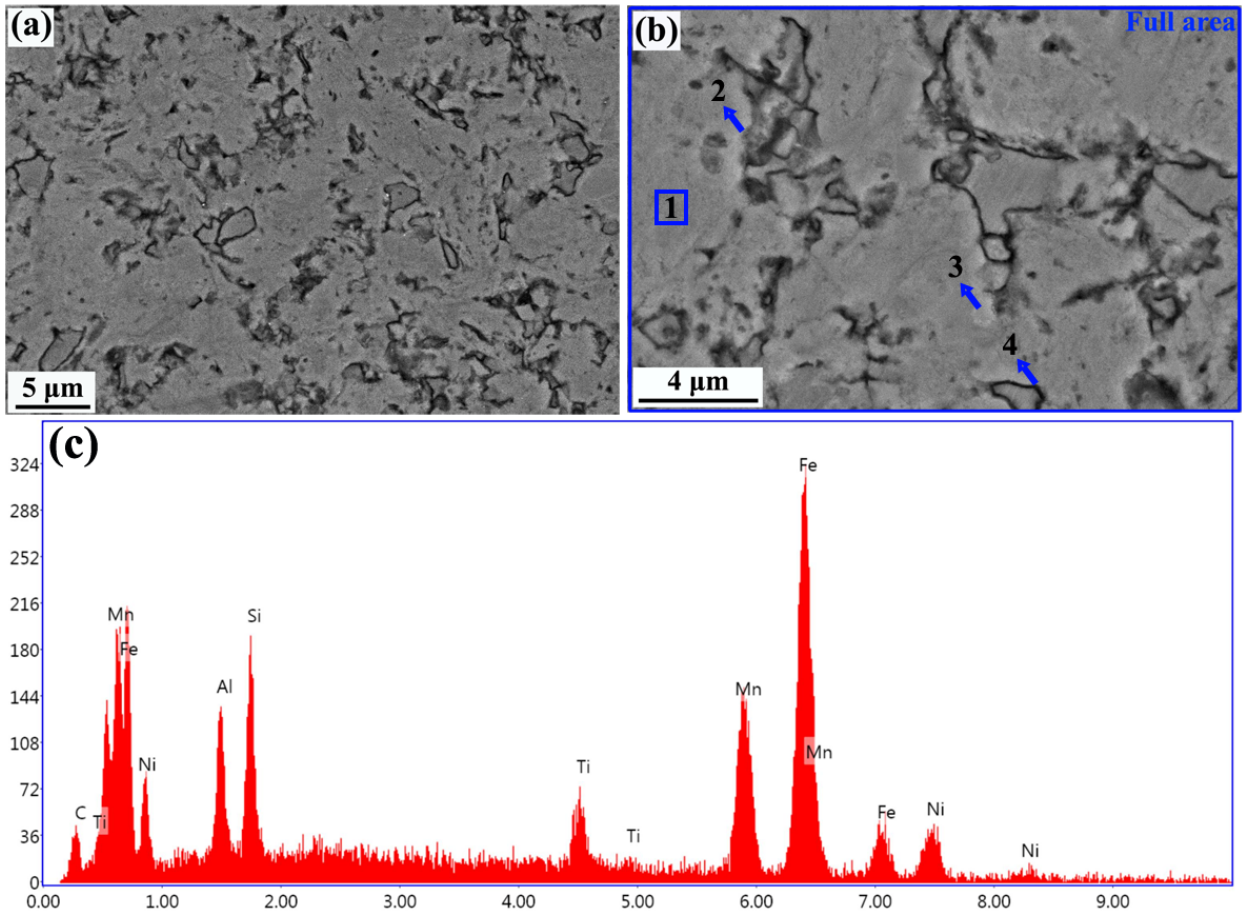

Figure 5.9: (a) and (b) SEM micrograph showing the microstructural features of the SPSed sample of the high entropy steel at different magnifications; (b) Microstructural region SPSed samples investigated for full area EDS analysis; (c) EDS spectrum corresponding to the full area scanning of the microstructure shown in (b). The light grey, dark grey, white and black contrast were marked as 1, 2, 3, and 4, respectively in (b).

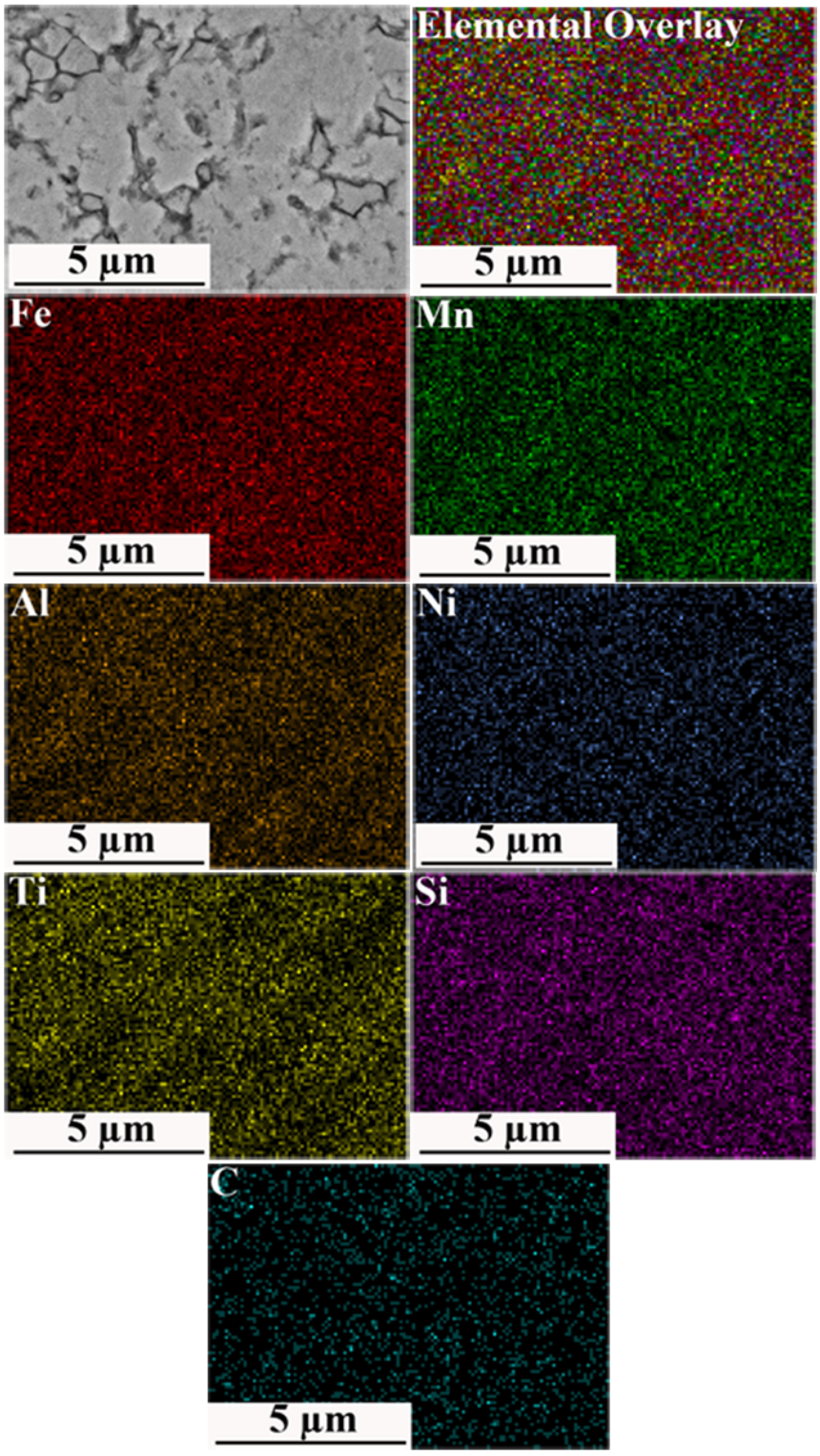

Figure 5.10: Elemental distribution and elemental overlay of SPSed sample of the HES3. Mapping shows the uniform distribution of the individual elements.

5.8 Physical and mechanical properties of the SPSed sample

The relative density of the SPSed sample achieved was ~ 99.7 %. The rule of the mixture was used to calculate the theoretical density and the Archimedes principle was used to calculate the experimental density (was repeated six times), and its calculation detail is mentioned in 2.5.1. The value of theoretical and average experimental density was found to be 6.18 g/cc and 6.16 g/cc, respectively.

The instrumented microhardness of the SPSed sample of non-equiatomic HES, as shown in Figure 5.11(a), depicts a load-displacement curve. Figure 5.11(b) shows the optical micrograph of the indent on the surface of SPSed HES at the load of 5000 mN. The depth of penetration was 5.18 μm corresponding to a load of 5000 mN. The values of the average microhardness and elastic modulus of the SPSed sample were obtained to be ~ 10.4 ± 0.2 GPa and ~ 209 ± 3 GPa respectively. The compressive engineering stress vs strain curve of the SPSed sample is displayed in Figure 5.11(c). The radar diagram is shown in Figure 5.11(d), which represents the comparison of various mechanical and physical properties. The values of compressive strength and strain were found to be ~ 2300 ± 100 MPa and ~ 15 %, respectively.

Figure 5.12(a, b, and c) shows the fractured surface of the SPSed sample, which clearly depicts the shallow dimple-like feature and cleavage facets. In the fractured surface, the shallow dimple like features is uniformly distributed, which shows that alloy have an appreciable amount of ductility. However, typical brittle fracture like features is also evident from the fractured image i.e., river-like patterns, cleavage steps, and cracks in the fracture surfaces. These differences in fracture patterns lead to different fracture morphologies. Both the ductile and brittle fracture features are observed in the fractured surface, which implies that the alloy have good strength with an appreciable amount of ductility.

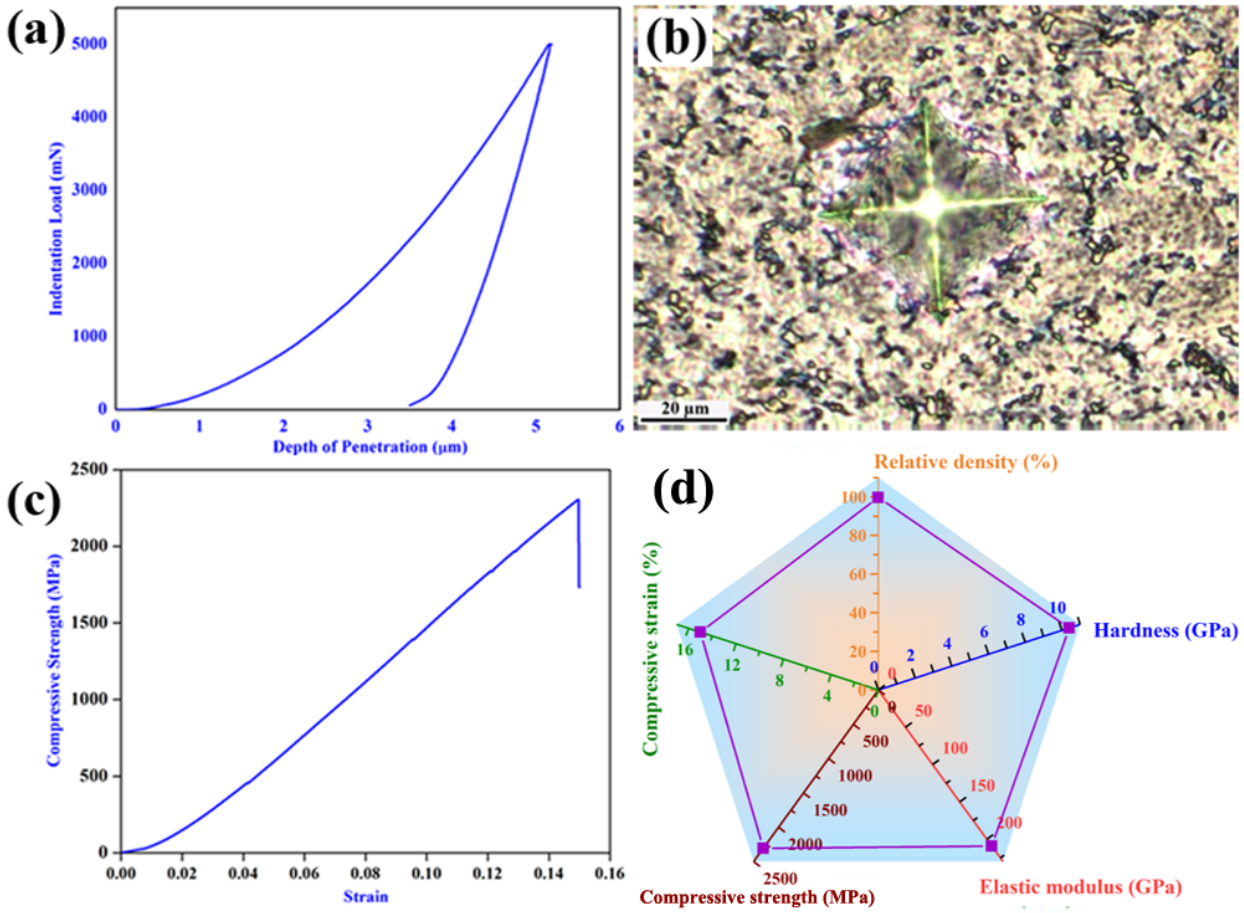

Figure 5.11: (a) Load-displacement (p-h) curve of SPSed sample of the non-equiatomic FeMnNiTiAlSiC high entropy steel; (b) Optical micrograph representing the indent on the surface of SPSed sample; (c) Engineering stress-strain curve of the SPSed sample under compression at room temperature; (d) The radar diagram manifests the physical and mechanical properties of the SPSed sample. The stress and strain curve reveals the ultimate strength and strain of the present alloy were ~ 2300 ± 100 MPa and ~ 15 %, respectively.

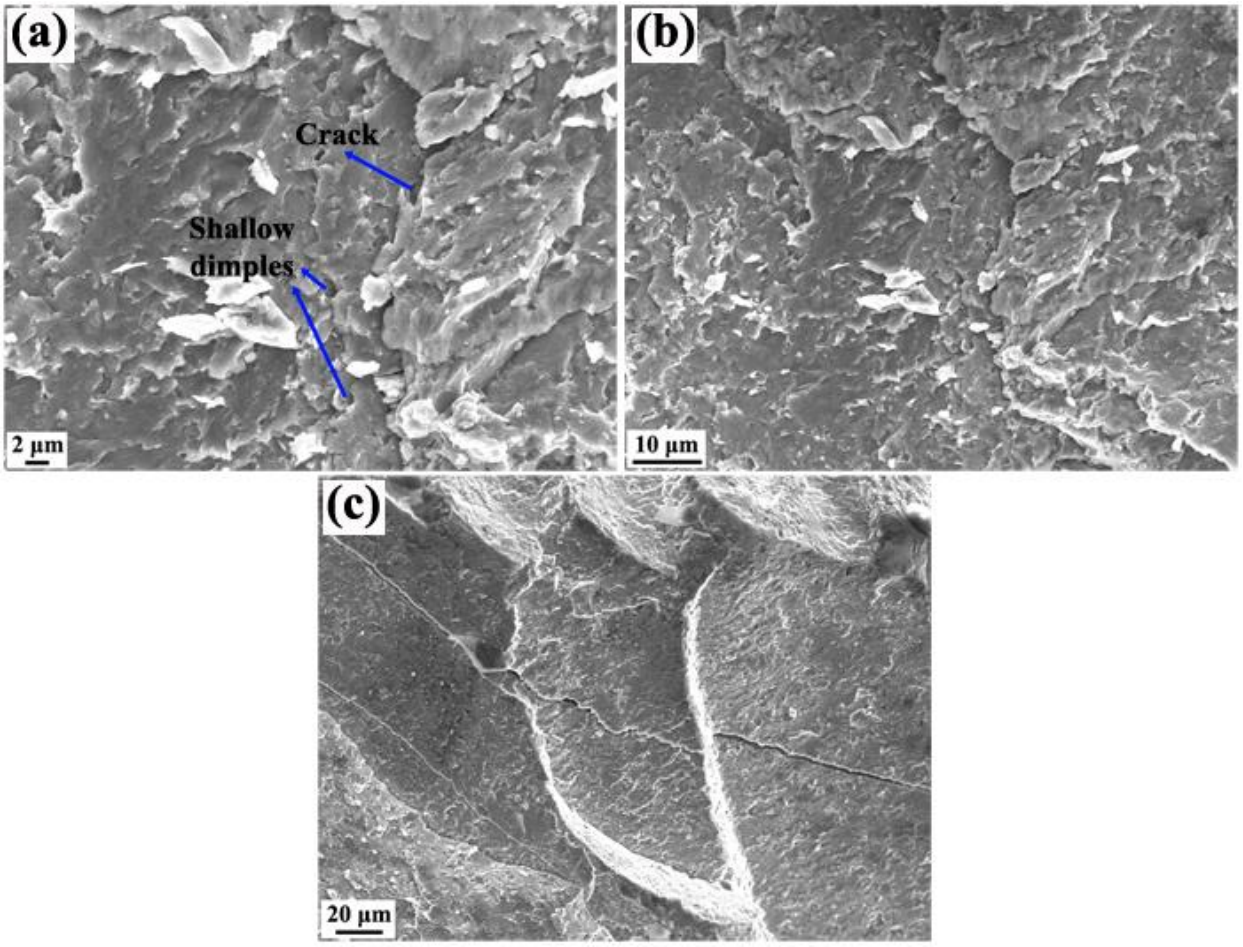

Figure 5.12: (a, b and c) SEM (SE) micrograph at different magnification of the fractured surface of SPSed sample of the HES3. The micrograph shown the shallow dimple and cracks features.

5.9 Wear behaviour of the SPSed sample

The average coefficient of friction and specific wear rate are essential characteristics of wear, which vary with applied normal load. This is evident from the plot (Figure 5.13(a)) of CoF vs time that CoF decreases with increase in load, and its values are found to be 0.12 ± 0.01, 0.29 ± 0.06, and 0.56 ± 0.03 for load conditions of 20 N, 10 N, and 5 N, respectively. It can also be seen that there are less fluctuations in CoF curves at relatively higher load. During the wear cycle the wear debris forms, accumulates, and segregates from the wear surface, resulting in fluctuation in the coefficient of friction. This kind of fluctuation is highest at 10 N load condition among all load

conditions. The CoF curve shows the sudden rise and then reaches the steady state condition at 5 N and 10 N load and it might be due to the breaking-in of the surface against the hard ceramic (Al_2O_3) during the wear. This kind of behaviour was also observed in previously reported HEAs and their composite [280, 281]. The high CoF at the low load condition might be due to the accumulation of wear debris in the wear track. The low CoF at high load condition is due to the removal of the wear debris from the wear track. The specific wear rate of the non-equiatomic high entropy steel was determined using the Archard equations, details are given in subsection 2.6.1. The values of the average specific wear rate of the SPSed sample, taken after the three reciprocating sliding wear tests done at each load condition, is found to be 3.25 x 10^{-5} mm^3/mN, 2.04 x 10^{-5} mm^3/mN and 1.62 x 10^{-5} mm^3/mN for 20 N, 10 N, and 5 N, respectively. Figure 5.13(b) illustrates the relation between the CoF and specific wear rate with the applied load condition.

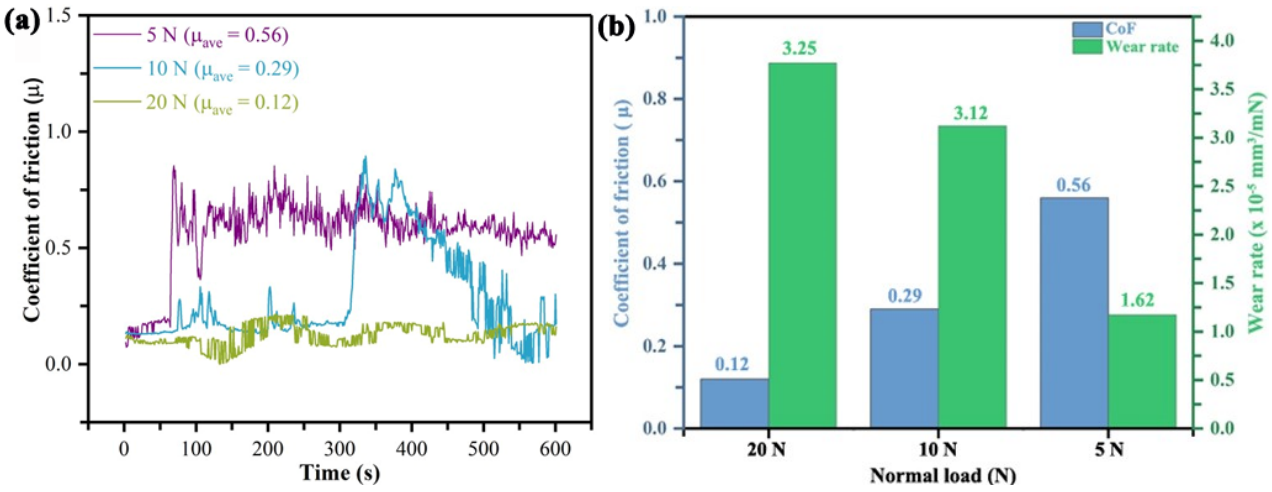

Figure 5.13: (a) Change in coefficient of friction as a function of time (s) for various normal load at 5 N, 10 N and 20 N of the SPSed sample; (b) Average coefficient of friction and specific wear rate against the various normal applied load.

The SEM was done on the worn surfaces of the SPSed samples of the non-equiatomic high entropy steel to understand the wear mechanism in detail. The SEM micrographs at different load of 5 N, 10 N, and 20 N are displayed in Figure 5.14 (a and b), (c and d), and (e and f), respectively.

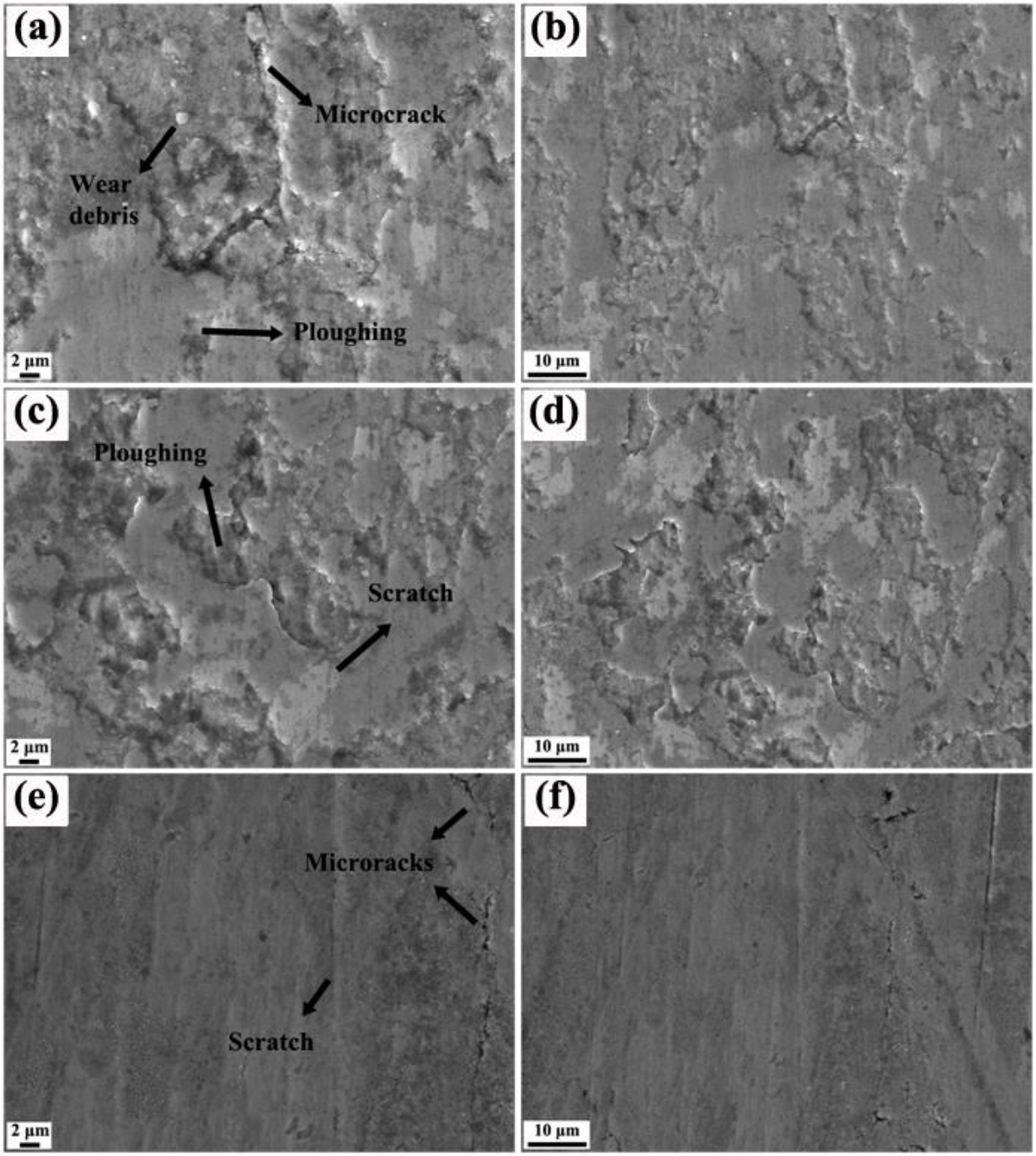

Figure 5.14: SEM (SE mode) micrographs at different magnification of wear fractured SPSed sample of the HES3; (a and b) at 5 N; (c and d) at 10 N and (e and f) at 10 N.

High-resolution micrographs of the worn surface ascertain many topological features, present. A smaller portion of the worn surface was covered by tiny debris, and ploughing grooves and several

well-defined delamination zones are also evident (Figure 5.14(a, c and e)). The ploughing of micro-asperities between two friction surfaces is the reason behind the development of the scratches in the wear track, which shows that abrasive type of wear mechanism is dominant. The accumulation of wear debris is observed in 5 N and 10 N load conditions. The black arrow is used to mark these features in the SEM micrograph of the worn surface (Figure 5.14). The SEM micrograph of the worn surface at 5 N, 10 N, and 20 N implies that the attack on the worn surface under the 20 N load condition is more severe as compared to the 5 N and 10 N load conditions. Further, at 20 N load conditions, the formation of microcracks is observed in a direction perpendicular to the sliding wear, as displayed in Figure 5.14(e), which is due to stick-slip behaviour at higher load conditions.

5.10 Biocompatibility of the SPSed sample

The in vitro biocompatibility of the HES3 was assessed based on the cell viability of MG-63 cell and compared with conventional 316L. As shown in Figure 5.15, there is a significant difference in the absorbance between the HES and 316L alloy samples, demonstrating that the cytotoxicity of the high entropy steel is far better than that of the as cast 316L stainless steel sample. The optical absorbance value was calculated from the viability of the living cell on the surface of the samples at a wavelength of 595 nm, using equation no. 2.6. As the incubation time increased, the cells proliferated continuously increasing in both the alloys, which is validated by the progressively-increased viability. Higher proliferation is perceived on the non-equiatomic HES as compared to the 316L. Thus, it can be concluded that the in vitro cell response of the present alloy is far better than that of the

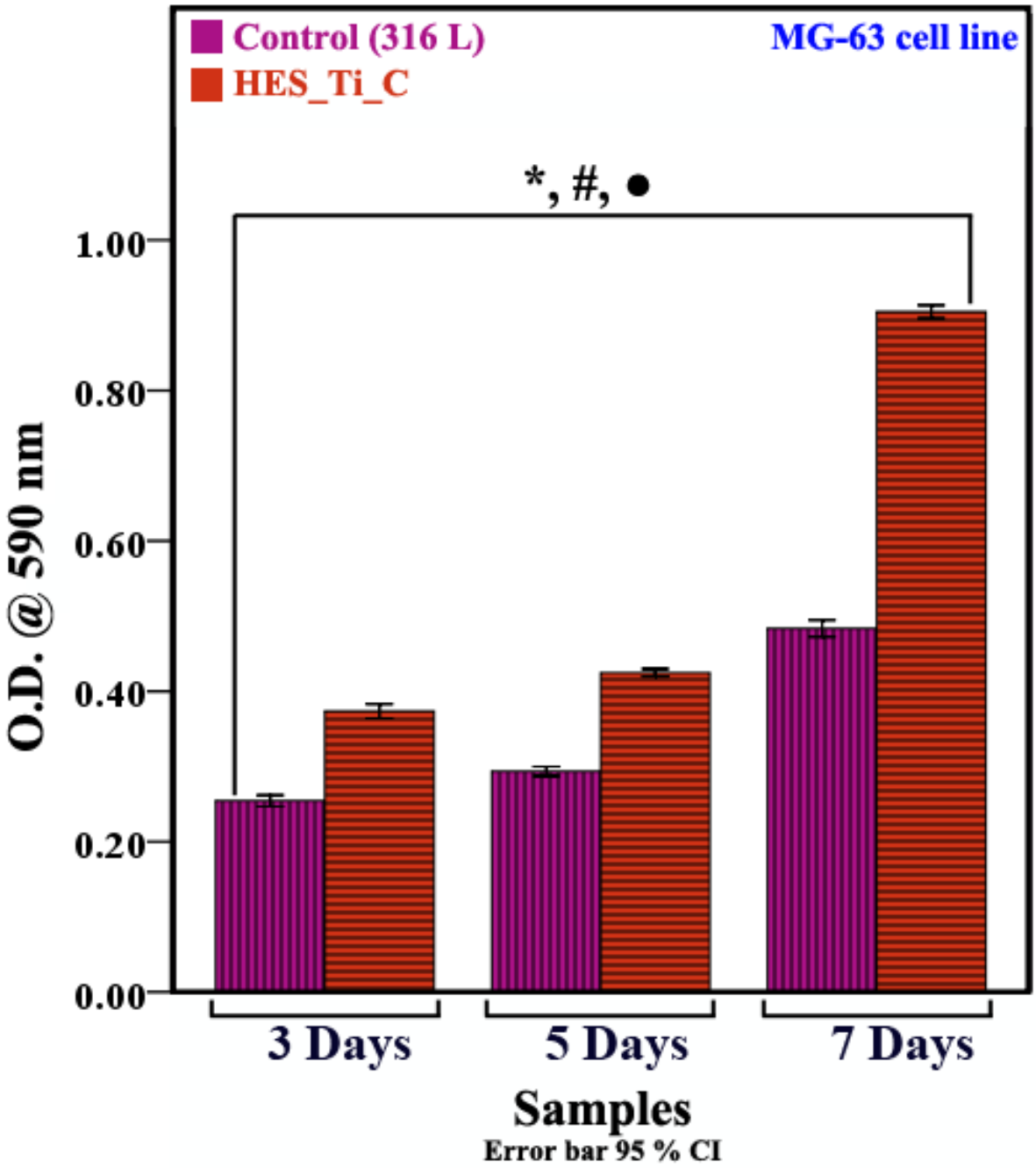

Figure 5.15: Quantitative assessment of cell density on SPSed and control (316L) specimens on mesenchymal stem cell (MG-63) after 3, 5, and 7 days. The symbol (*) signifies that the statistically difference in the mean optical density (O.D.) among the SPSed sample of the HES3 with the control sample (316L) treated for 3 days with 5 and 7 days of control and HES3 samples. The symbol (#) denotes the statistically differences in the O.D. among all the sample, treated for 5 days as with sample treated for 7 days. The symbol (●) symbolises the statistically differences in the O.D. among all the sample treated for 7 days with HES3 sample.

control. The value of mean optical density ($p \leq 0.05$) for the non-equiatomic FeMnNiTiAlSiC high entropy steel is found to be 1.46, 1.50 and 3.08 % for 3-, 5- and 7-days incubation periods, respectively. The improved biocompatibility of the alloy system can be attributed to the presence of elements like Ti and Si. It is well known that Ti has excellent bioactivity, and better tolerated in 3T3 mouse fibroblasts in 316L which has already been reported [261, 282]. So, the cumulative effect of the Ti and Si is the reason behind the better biocompatibility in this alloy system.

5.11 Discussion

5.11.1 Phase evolution and formation

The phase evolution during the mechanical alloying and spark plasma sintering was understood with the help of thermodynamic parameters. The Gibbs phase rule suggests that the phases formed depend upon the equation given as, $P + F = C + 1$ for the alloys where, P = no. of phases, F = degree of freedom, and C = no. of components. The other condition (assuming $F > C + 1$) was applicable when the process of phase formation was not in equilibrium conditions. The phases formed after the milling and SPSed sample showed fewer phases than expected. The HEAs sometimes do not follow the Hume-Rothery rule to predict phase formation.

The high configurational entropy in HEAs favours the formation of solid solutions rather than intermetallic compounds. Besides configurational entropy, some other parameters were also proposed to predict the phase formation in HEAs i.e., mixing enthalpy (ΔH_{mix}), atomic size mismatch (δ), electron concentration (VEC) and Ω parameter, and details of the calculation are given in section 1.5. The calculated values of all the parameters are listed in Table 5.4. The value of the atomic size mismatch was not in the range of solid solution formations. The VEC parameter for the present alloy lies in the range of a single BCC solid solution, and it forms the BCC solid

solution during 30 h of milling. In the present condition, the enthalpy of mixing and atomic size mismatch might be the dominant factor.

Table 5.4: Thermodynamic parameters values of the HES3.

Thermodynamic parameter	ΔH_{mix} (kJ/mol)	ΔS_{conf} (J/K-mol)	δ (%)	**Ω**	VEC
Present work	-10.7	13.44	8.5	2.0	6.47

The phase formation after the milling was also correlated with the physicochemical properties of the individual element's values which are listed in Table 2.3. The major phase formed during the milling was BCC (α-Fe as host lattice). The concept of host lattice was explained in terms of bond strength and the melting point of the elements present in the multicomponent alloys [242]. Si remains undissolved after the milling which may be attributed to the self-diffusion parameter of the alloying elements in the HEAs [240]. The self-diffusion coefficient of Si in the present condition was the lowest among all the other alloying elements present (Table 2.3). The phases formed after the sintering were the dual-phase structure (FCC + B2-type) along with some intermetallics i.e., TiC and Fe_5Si_3 type phase. The binary enthalpy between the Fe-Mn was ~ 1 kJ/mole which was within the limit of the solid solution formation. The electronegativity and atomic radius of Fe and Ni were close to each other which favours the formation of a solid solution. This might be the reason for the FCC solid solution enriched in Fe, Ni, and Mn. The formation of the B2-type phase is due to the binary enthalpy between the Fe-Al and Ni-Al being highly negative, as shown in Figure 5.16. The formation of TiC intermetallics was due to the difference in the atomic radius of the element with Ti. Moreover, Ti has a higher affinity towards carbon [283]. The

binary enthalpy between Fe and Si was highly negative which might be held responsible for the formation of the Fe_5Si_3 type intermetallic phase, as displayed in Figure 5.16.

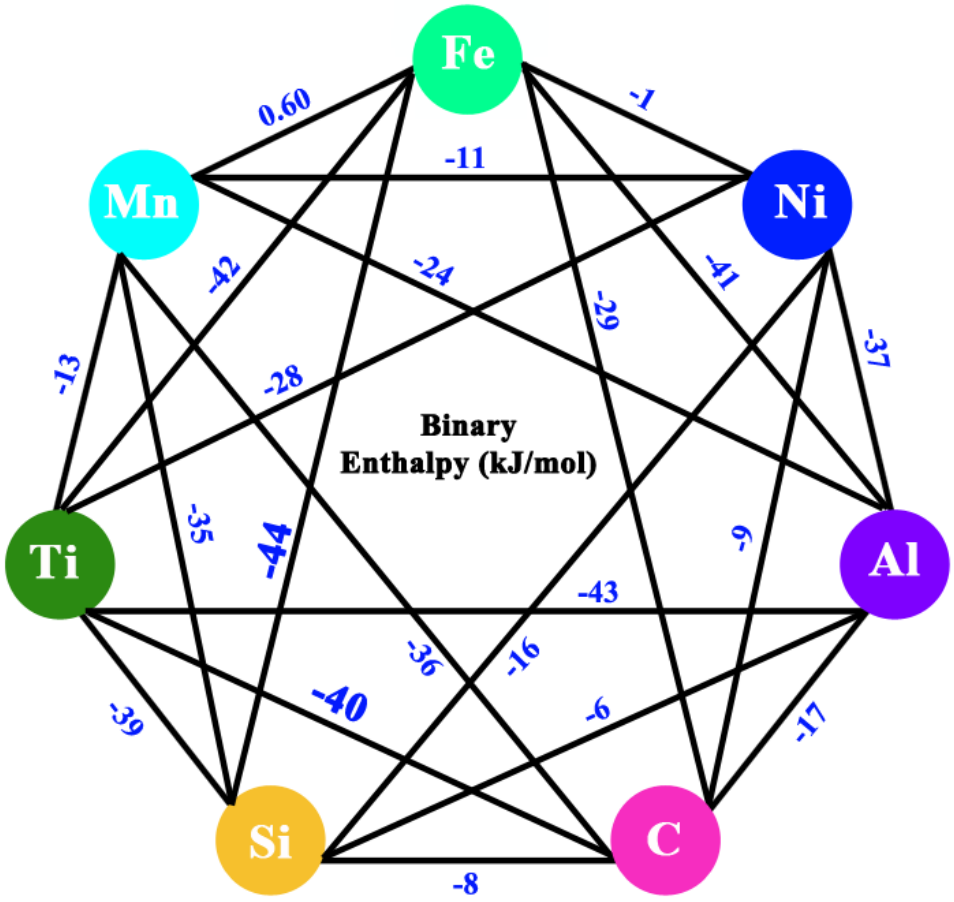

Figure 5.16: Binary enthalpy (kJ/mol) values of all the binary pairs in the non-equiatomic FeMnNiTiAlSiC HES.

The broadening and decrease in intensities of the diffraction peaks of the phases were due to the usual characteristics of mechanical alloying. The effect on the crystallite size, lattice strain, and dislocation density with milling time was discussed. The induced lattice strain increased, and simultaneously the crystallite size decreased with a certain duration of milling time. The increase in lattice strain generally observed in the early duration of the milling time, is due to three factors, i.e., (i) the effect of atomic radius mismatch between the individual elements, (ii) an increase in the fraction of grain boundary with progressive milling and (iii) mechanical deformation of powder

particles. The rapid decrease in crystallite size is generally at the start of the milling time due to the high impact force and transfer of high kinetic energy to the powder particles. This also induces high dislocation density which gives rise to work hardening in the powder. The contribution of the impact force reduces grain refinement as the milling progresses. Therefore, the prolonged duration of milling does not significantly contribute to the crystallite size refinement and enhancement of lattice strain [278]. It can be noted that the dislocation density shows negligible changes after 20 h of milling due to the fact that the crystallite size and lattice strain were reaching near saturation [277]. This kind of behaviour was also reported in the HEA [137] and Al-CNT composite [284] produced through mechanical milling.

5.11.2 Thermal Stability

The phase transformation events shown from the DSC and ex-situ XRD of the annealed sample of the non-equiatomic high entropy steel were discussed and correlated with the property diagram predicted from CALPHAD modelling, as follows:

- At R.T.; BCC + γ-brass type + Si.
- At 500 ℃; BCC + γ-brass type. The alloy was thermally stable up to 500 ℃.
- At 600 ℃; some additional peaks were visible which correspond to an ordering and texturing of the γ-brass type phase at higher temperatures, this kind of ordering or texturing of the phases was observed in the HEAs [148] and quasicrystal [243].
- At 900 ℃; the γ-brass structure dissolves and the formation of FCC (austenite) solid solution evolves along with the intermetallics TiC and Fe_5Si_3 type. This phase formation could be related to the exothermic events at 690 ℃ and 860 ℃. This is due to the diffusion kind of phase transformation, and it's also observed in the previously reported HEAs [107]. The formation of the TiC carbide was due to the higher enthalpy of binary mixing between

Ti-C, and its tendency of carbide formation (Ti) with C is previously reported in the HEAs [283]. The formation of the Fe_5Si_3 type of silicide might be due to the undissolved Si after the milling and the binary negative enthalpy between the Fe-Si and Mn-Si.

- At 1100 ℃; it was observed that no new phases evolved, but the amount of phase fraction between the BCC and FCC phase changes drastically which might explain the exothermic event at 1000 ℃.

The property diagram of the alloy was shown in Figure 5.17 generated by the ThermoCalc software using CALPHAD modelling. The CALPHAD result shows that the liquid forms (98%) approximately at 1200 ℃ which contains Fe, Mn, Ni, Al, and Si except for TiC (2%). The phases formed from liquid around 1100 ℃ were BCC_A2#1 phase (rich in Fe, Al, and Mn) along with the intermetallic TiC (rich in Ti, and C), as shown in Figure 5.17 (b and d), respectively. The number of phases remains unaltered up to 800 ℃, and after this, the FCC_A1#2 phase formed (contains Fe, Ni, Mn, and Al), as displayed in Figure 5.17(e). At 300 ℃ the BCC_A2#2 phase formed which was enriched in Mn, Fe, Ni, and Al as shown in Figure 5.17(c). Figure 5.17(b-f) shows the elemental composition in all the phases and their stability with respect to temperature.

The phases formed after the milling were BCC and γ-brass type (Cu_5Zn_8) structures were correlated with the predicted phases from CALPHAD results. The phases formed after the isothermal annealing and sintering were somewhat close to the predicted phases from the CALPHAD (Thermocalc) modelling. Some differences in the phase prediction (Thermocalc) and experiment phases were due to the limitation of the CALPHAD database (TCHEA) for the CALPHAD modelling.

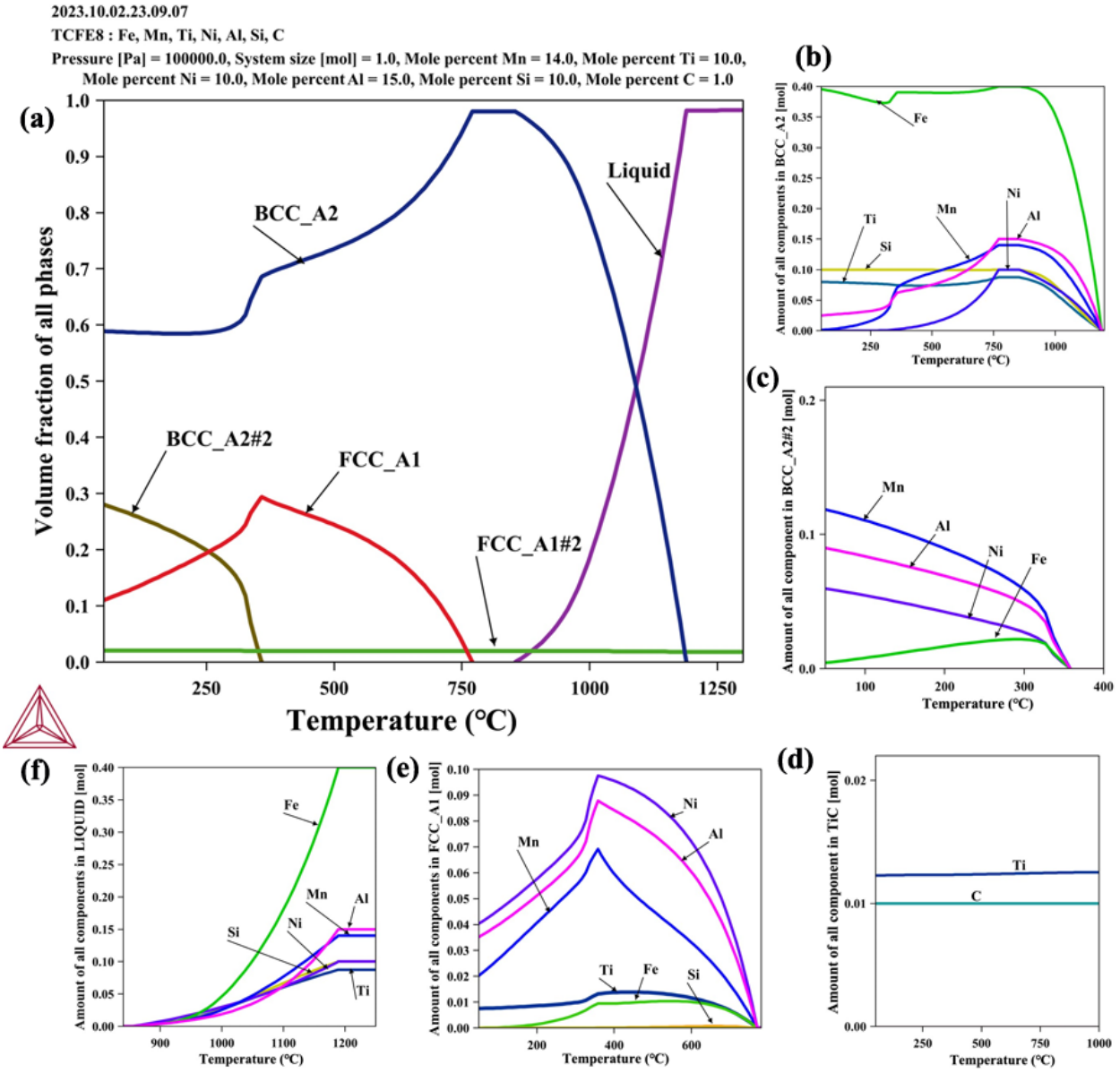

Figure 5.17: (a) Property diagram of the non-equiatomic FeMnNiTiAlSiC high entropy steel; (b-f) The elemental composition in all the phases and their stability with respect to temperature.

5.11.3 Strengthening Mechanism

The value of microhardness and yield strength of the present alloy was found to be 10.4 ± 0.2 GPa and 2300 ± 100 MPa, respectively. The yield strength of the alloy was due to the overall effect of frictional stress (σ_o), grain boundary (σ_{gb}), dislocation (σ_d), precipitation (σ_p), and solid solution strengthening (σ_{ss}), and the equation is given in equation no. 1.9.

In the SPSed sample, very fine grains formed due to the processing technique (MA followed by SPS) as compared to many wrought HEAs. The high-volume fraction of grain boundaries can impede the dislocation motions and thus improve the mechanical properties. The grain boundary strengthening was expressed by the Hall-Petch relationship which is expressed in equation no. 1.13, and the value of the k_y is listed in Table 5.5, and d = grain size diameter of FCC and B2-type phases which was 1.31 μm and 0.36 μm, respectively. The values found for the FCC and B2-type phases were 719 MPa and 963 MPa, respectively.

The dislocation present in the alloy impedes the movement of dislocation because the dislocations interact with each other and restrict their motion. Thus, increasing the dislocation density in an alloy as a result yields strength increase. The dislocation strengthening was given in equation no. 1.12. The value of M = Taylor factor, G = Shear modulus, α = constant, and ρ_D = dislocation density, is listed in Table 5.5. The microstrain and crystallite size for FCC and B2-type phases are 0.42 % and 36 nm, 0.34 % and 42 nm, respectively. The values of the dislocation strengthening for the FCC and B2-type phases were 576 MPa and 553 MPa, respectively.

The precipitation strengthening due to the carbide and silicide formation on the strength of the alloy was estimated by equation no. 1.14 and 1.15. The values of the various terms used in the equation are, f = volume fraction of carbides, r = mean radius, and λ =distance between the precipitates. The mean radius and weight fraction of carbide, and silicide are 96 nm and 11.10%, 81 nm and 9.50 %, respectively. The strengthening due to the carbide and silicide precipitation for the FCC and B2-type phases was calculated to be 220 MPa and 230 MPa, and 195 MPa and 206 MPa, respectively. Due to the high compressive strength of the alloy other than carbide and silicide

Table 5.5: Physical meaning and values of different symbols used in the strengthening mechanism calculations.

Symbol	Meaning	Values	References
σ_0	Frictional stress	95.4 MPa for FCC, and 120 MPa for B2-type	[225, 285]
k_y	Hall-Petch slope ($MPa/\mu m^{1/2}$)	823 for FCC, and 578 for B2-type	[225, 285]
M	Mean orientation factor (Dimensionless)	3.06 for FCC, and 2.73 for B2-type	[225, 285]
α	Constant (Dimensionless)	0.2 for FCC and B2-type	[225]
b	Burger's vector	Details given in subsection 2.3.1	This work
ρ_D	Dislocation density	$\rho_D = 3.4 \times 10^{15}$ m^{-2} (FCC), and $\rho_D = 4.2 \times 10^{15}$ m^{-2} (B2-type)	This work
G	Shear modulus (GPa)	63.07 GPa (Rule of mixture)	This work
υ	Poisson ration (Dimensionless)	0.3	This work

particles the B2-type phase was also considered as a dispersoid for the dislocation of the FCC phase. The effect of the B2-type phase particles on the FCC phase was calculated from equation no. 1.14 and 1.15, and its value was found to be 116 MPa.

The Fleischer model was given to calculate the solid solution strengthening of the alloy, which is given in equation no. 1.10 and 1.11. The values of the termed used in the equation are M = Taylor constant, G = shear modulus, and value listed in Table 5.5, c = percent of the solute atom, and ε_f = relation parameter.

In the present alloy, the dual-phase was formed i.e., FCC as the major phase and B2-type as the minor phase. The Al, Mn, and Ti were assumed to be the solute atoms for the FCC phase and Mn as the solute atom for the B2-type phase. The actual atomic percentage (from SEM-EDS) of the elements in the corresponding phases is mentioned in Table 5.3. The calculated values found for the solid solution strengthening for FCC and B2-type phases were 245 MPa and 72 MPa, respectively.

The phase fraction of the FCC and B2-type phases were found to be 58.0 % and 21.4 % respectively. The calculation of the strengthening mechanism was performed assuming the presence of only FCC and B2-type phases. Therefore, the contribution of the strengthening mechanism for the FCC and B2-type phases was determined as 73 % and 27 %, respectively. It was observed that the FCC phase strengthening primarily depends upon the grain boundary, dislocation, and precipitation strengthening. The values of the individual strengthening mechanisms in the phases are shown in Figure 5.18(a), and their contribution in percentage is displayed in the pie chart, which is illustrated in Figure 5.18(b).

The experimental yield compressive strength (2300 ± 100 MPa) was higher than the calculated strength (2179 MPa). The difference may be due to the minor contribution of twin boundary strengthening (not calculated) in the present alloy and the heterogeneous kind of structure present in the alloy which would not be considered during the calculation. This kind of difference had shown in previous studies also that the back stress generation happened due to the heterogeneous structures [225]. To compare the mechanical properties of the present alloy with the reported Fe-based HEAs, high entropy steel and conventional steel were mentioned in Table 1.3. The data were based only on the room temperature mechanical properties i.e., microhardness and compressive strength. The comparison shows that the alloy exhibits a better combination of high strength and

low density as compared with other HEAs. The present investigation on the high entropy steel suggests that the mechanical properties obtained were very promising.

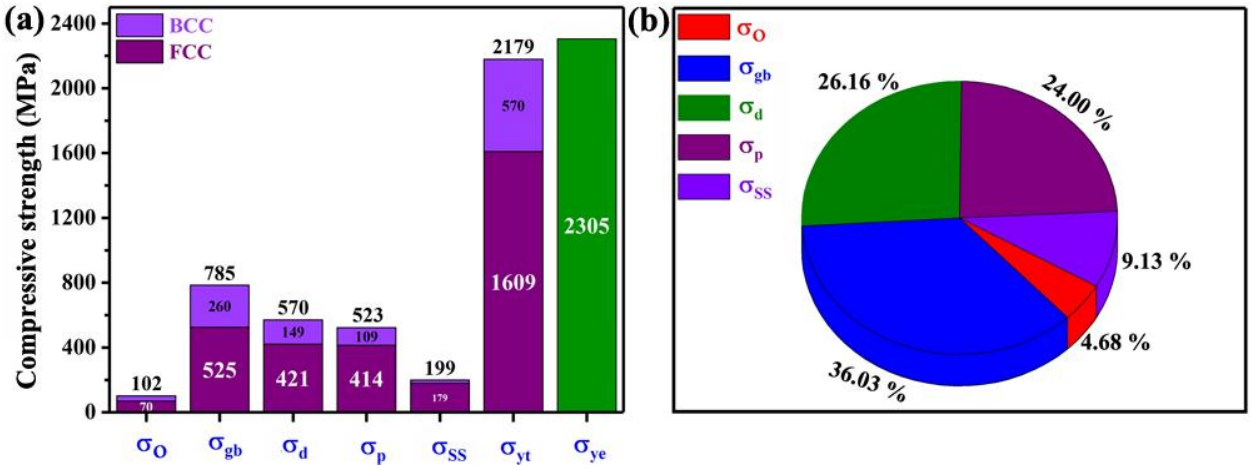

Figure 5.18: (a) Individual contribution of the various strengthening mechanism for FCC and B2-type phases, and experimental yield strength; (b) Percentage of the individual strengthening mechanism in the HES3.

5.11.4 Wear behaviour and mechanism

The fluctuation in the coefficient of friction with respect to time at low load conditions might be due to the continuous production and separation of wear debris from the wear track. Further, the wear debris is stuck to the worn surface and sometimes develops local cracks in the wear track; this results in the fluctuations of CoF. The formation of the FCC and B2-type with the hard intermetallic precipitates gives rise to the excellent strength and good ductility. The alloy also possesses low coefficient of friction and specific wear rate. Due to the formation of a hard B2-type intermetallic, some localized microcracks are observed in the worn surface particularly evident at high load conditions (20 N), this happened due to brittleness in the alloy. This kind of observation at higher load was also evident in the previously reported HEAs in which the B2-type phase was present [173, 274, 280]. This alloy showed excellent wear resistance as compared to previously reported HEAs and conventional steel [283,286]. This alloy has excellent mechanical properties

i.e., microhardness and compressive strength with an appreciable amount of ductility making it a potential candidate for high temperature structural application. Further, the alloy shows low elastic modulus, higher mechanical properties, good wear resistance, low density, and better biocompatibility as compared to conventional 316L. This makes it a potential candidate for biomaterial applications. Systematic studies are required to understand the biocompatibility behaviour in this alloy system i.e., bio tribology, bio corrosion, antibacterial, and leaching behaviour, for future application of this alloy as a biometallic alloy.

5.12 Conclusions

The HES3 was synthesized by MA and sintered by SPS. The alloying behaviour, thermal stability, and mechanical properties were systematically investigated. The conclusions that can be drawn from the present investigation are as follows:

1. The phases formed after 30 h of milling were dual-phase structures with BCC (a = 0.287 nm), and γ-brass type (a = 0.890 nm) solid solution along with a minor amount of undissolved silicon.
2. The DSC result shows four exothermic events which confirms that the phase transformation occurred upon heating of the as-milled sample up to 1050 ℃. The alloy was thermally stable up to 500 ℃ and afterward showed the evolution of FCC solid solution along with the intermetallics i.e., TiC and Fe_5Si_3. This finding was very well correlated with the ex-situ XRD of the annealed samples at various temperatures.
3. The mechanical properties of the SPSed sample i.e., microhardness, elastic modulus, and yield compressive strength were evaluated to be ~ 10.4 ± 0.2 GPa, ~ 209 ± 3 GPa, and ~ 2300 ± 100 MPa respectively, due to the presence of B2-type secondary phase coexisted with carbide and silicide as nanoprecipitates. The various strengthening mechanisms for

the alloy were evaluated and it seems that the high strength was mainly due to the grain boundary, dislocation, and precipitate strengthening.

4. The semi-empirical thermodynamics parameters of the present alloy were ΔH_{mix} = -10.7 kJ/mole, δ = 8.5 %, and ΔS_{conf} = 13.44 J/K-mole, which were not in the range of solid-solution formation criteria of HEAs. The phases formed after the isothermal annealing and sintering were a dual-phase structure with some intermetallics which might be due to differences in atomic size and unfavourable enthalpy of mixing in some pairs.
5. This high entropy steel showed excellent wear resistance against the hard ceramic counter ball (Al_2O_3), and the values of the lowest specific wear rate are found to be 1.62 x 10^{-5} mm^3/mN. The dominant wear mechanism in this high entropy steel is abrasive wear.
6. This alloy showed better cell proliferation and adhesion in the MG-63 cell line after 3, 5, and 7 days as compared with the 316L. The better mechanical, wear and biocompatibility as compared with 316L makes it as a potential candidate for bioimplant applications.